JMEPEG (2018) 27:4507–4513
https://doi.org/10.1007/s11665-018-3542-0

1059-9495/$19.00

Microstructure and Electrochemical Performance of $CeMg_{12}$/Ni/TiF_3 Composites for Hydrogen Storage

Feng Hu, Yongzhi Li, Jianyi Xu, and Yanghuan Zhang

(Submitted April 16, 2017; in revised form May 5, 2018; published online August 1, 2018)

Ball milling was used to prepare $CeMg_{12}$/Ni/TiF_3 composite alloys in this study. Microstructures of experimental alloys were analyzed by scanning electron microcopy (SEM), x-ray diffraction (XRD), and high-resolution transmission electron microscopy (HRTEM) with electron diffraction (ED). The electrochemical and kinetic characteristics of the ball-milled composite alloys were further evaluated based on their galvanostatic charge–discharge measurement, high-rate dischargeability (HRD), hydrogen diffusion behavior, as well as electrochemical impedance spectrum (EIS). Results indicated that the ball-milled alloy with 3 wt.% TiF_3 exhibited the best electrochemical discharge capacity, which was not only related to the formation of amorphous and/or nanocrystalline phase but to the formation of MgF_2 because it can effectively reduce the thermodynamic stability of hydride. With increasing TiF_3, the cycle degradation rates of the milled alloys were ameliorated remarkably. This improvement was attributed to the formation of an amorphous phase (which possesses strong anticorrosive and antioxidation abilities) as well as the formation of MgF_2 and TiNi secondary phases. The ball-milled alloy with 3 wt.% TiF_3 additive exhibited the strongest electrochemical kinetic properties, related to the highest hydrogen diffusion rate in the alloy (which was associated with multiple defects and grain boundary of amorphous and/or nanocrystalline phases) and the electrochemical reaction on the surface of alloy (which was related to the lowest apparent activation energy).

Keywords activation energy, amorphization, cycling life, electrochemical impedance spectroscopy, nanostructured materials

1. Introduction

Magnesium (Mg)-based hydrogen storage alloy materials have been recently regarded as the most promising negative electrode materials because of their higher hydrogen storage capacity, lightweight, and abundant raw materials (Ref 1, 2). Meanwhile, the inferior kinetic performance and high-temperature hydriding and dehydriding reaction for Mg-based alloys confers a reduced electrochemical charge and discharge capacity (Ref 3, 4). A large number of studies on Mg-based hydrogen storage alloys indicate that prompting the formation of nanocrystalline and/or amorphous structures inside alloys by ball milling with Ni powders can significantly improve the absorptive and desorptive properties of Mg-based alloys. Such alloys can store and release hydrogen at ambient temperatures and pressure (Ref 5, 6). Lei et al. (Ref 7) synthesized an amorphous Mg-Ni alloy by mechanical alloying, which exhibited high discharge capability. Zhang et al. (Ref 8) systematically investigated the change in the electrochemical capability of the ball-milled $(Mg_{1-x}Zr_x)_2Ni$ ($x = 0$, 0.3) under the assumption that substituting Zr for Mg and prolonging the milling duration can enhance the electrochemical discharge capacity as well as cycle stability.

Compared with the Mg-Ni alloy, the rare-earth (RE)-Mg series alloy can be potentially used as a hydrogen storage material because of its considerably higher hydrogen storage capacity (3.7-5.5 wt.%) (Ref 9, 10). The discharge capacity of the La_2Mg_{17}- and $LaMg_{12}$-type alloys prepared by mechanical ball milling reached 990 mAh/g (Ref 11). Pure RE_2Mg_{17} alloy hydride showed poor hydriding/dehydriding kinetic performance because of its high thermodynamic stability. Metallic Ni particles were dispersed throughout the RE-Mg alloy matrix by milling with Ni, which effectively improved the electrochemical discharge property of the hydrogen storage alloy (Ref 12). Wang et al. (Ref 13) indicated that alloys added with Ni powders could markedly improve the discharge capacity of ball-milled $NdMg_{12}$-type alloys. Compared with the aforementioned method, adding transition metal fluoride as a catalytic agent could effectively improve the absorption/desorption properties of alloys. The formation of MgF_2 in the ball-milled MgH_2 with transition metal fluoride could effectively enhance the hydrogen releasing capacity of MgH_2 hydrogen storage materials (Ref 14, 15). Jin et al. (Ref 16) systematically investigated the catalytic effect of transition metal fluoride (FeF_2, NiF_2, TiF_3, NbF_5, and so on) on MgH_2 to verify that metal fluoride was an ideal catalyzer that can improve its reversible hydriding and dehydriding ability.

In previous reported literature, we mainly investigated the effect of changing of thermodynamic parameters on the electrochemical charge–discharge performance of $CeMg_{12}$-Ni-TiF_3 composite electrode materials in the study of the evolution of microstructure (Ref 21). In the present study, the microstruc-

Feng Hu, Department of Functional Material Research, Central Iron and Steel Research Institute, Beijing 100081, People's Republic of China; and School of Materials and Metallurgy, Inner Mongolia University of Science and Technology, Baotou 014010, People's Republic of China; **Yongzhi Li** and **Yanghuan Zhang**, Department of Functional Material Research, Central Iron and Steel Research Institute, Beijing 100081, People's Republic of China; and **Jianyi Xu**, School of Materials and Metallurgy, Inner Mongolia University of Science and Technology, Baotou 014010, People's Republic of China. Contact e-mail: hufengnhm_001@163.com.

ture of $CeMg_{12}/Ni/TiF_3$ composite electrode alloys was further explored. Meanwhile, the activation energy E_a could be calculated by fitting the electrochemical impedance spectrum (EIS) to elucidate the varying electrochemical kinetic capabilities of alloy samples under different conditions.

2. Experimental Methods

The $CeMg_{12}/Ni/TiF_3$ composite hydrogen storage electrode materials were synthesized by mechanically milling $CeMg_{12}$ alloy powders (pulverized to 200 mesh), nickel powders (the mass percentage was controlled at 100% of the $CeMg_{12}$ alloy), and TiF_3 (the mass percentage was controlled at x% of the $CeMg_{12}$ alloy, where x = 0, 3, 5) by using a planetary-type ball mill (QM-SP3). The rotational speed, mass ratio of ball to powder, and ball milling time were set to 350 rpm, 40:1, and 60 h, respectively. During mechanical milling, Ar gas was used to protect the atmosphere, thereby preventing the composite hydrogen storage material from being oxidized. In the discussion of the experimental results, the alloys are denoted as A_0, A_3, A_5 with TiF_3 content.

The phase structure and the composition of the composite materials were analyzed by x-ray diffraction using JADE 6.0. The prepared alloys were characterized by scanning electron microscopy (Philips QUANTA 400). The grain morphology and crystalline characteristics of the ball-milled alloys were observed by HRTEM and ED, respectively.

Cold-pressing was used in the preparation of the alloy electrode. The mass ratio of the composite materials to the carbonyl nickel powders, diameter, pressure, as well as the total weight of the electrode were limited to 1:4, 10 mm, 25 MPa, and 1 g, respectively. Testing of the electrochemical discharge capacity was conducted using a standard three-electrode system. Charge/discharge current density and discharge cutoff voltage were controlled at 40 mA/g and − 0.5 V.

The high-rate dischargeability (HRD) of different charge–discharge current densities, which was regarded as an important parameter, was used to evaluate the electrochemical kinetic properties and can be calculated using Eq 1, as follows:

$$HRD = C_d/C_{40} \times 100\%, \quad \text{(Eq 1)}$$

where C_d and C_{40} are the discharge capacity at the charge–discharge current density I_d and 40 mA/g (I_{40}).

Electrochemical alternating current (AC) impedance spectroscopy and potentiodynamic polarization plots of electrodes were measured using the PARSTAT2273 potentiostatic workstation for electrochemistry. The frequency ranged from 5 mHz to 10 kHz, and the AC amplitude was set to 5 mV. The measuring potential range was − 1.5 to 0.5, and the scan rate was fixed at 5 mV/s while testing the potentiodynamic polarization curves.

3. Results Analysis

3.1 Microscopic Characterization

The SEM photographs together with the typical EDS spectra of ball-milled A_0, A_3, A_5 alloys are presented in Fig. 1. The A_0

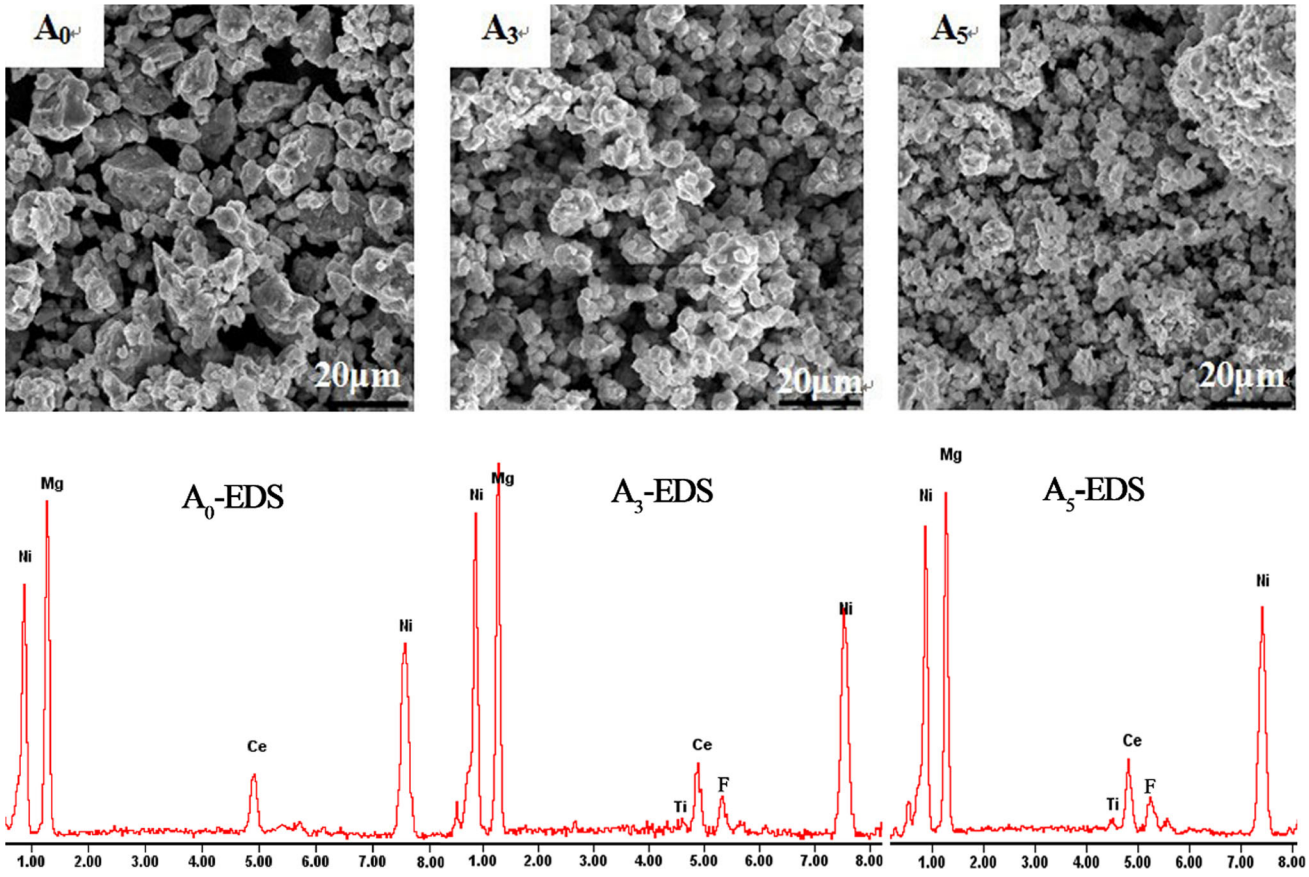

Fig. 1 SEM and EDS micrographs of A_0, A_3, A_5 alloys milled for 60 h

alloy consists of Mg, Ni, and Ce; the A_3, A_5 alloys are made up of a small quantity of Ti and F except for Mg, Ni, and Ce. Apparently, the size of the alloy particles decreases at varying degrees with increasing TiF_3 content, indicating that TiF_3 facilitates the refinement of alloy particles. The decrease in particle size leads to an increase in specific surface area, which increases the diffusion path of hydrogen atoms and the contact opportunity between the alloy particles and hydrogen atoms, thereby improving the hydriding/dehydriding reaction.

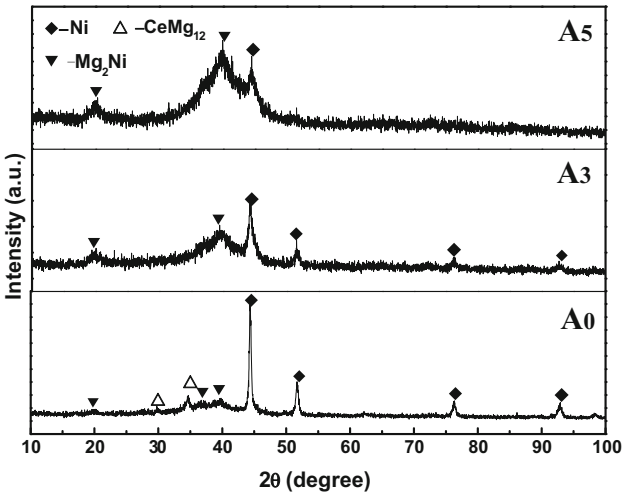

Fig. 2 XRD patterns of A_0, A_3, A_5 alloys ball-milled for 60 h

The XRD patterns of the ball-milled A_0, A_3, A_5 alloys are presented in Fig. 2. The milled alloys clearly exhibit multi-phase structures, consisting of the main phases Mg_2Ni (PDF# 75-1249), $CeMg_{12}$ (PDF# 19-0291), and Ni (PDF# 89-7128). Other amorphous phases may be hidden in scattered peaks, undetected by XRD analysis. The sharp and narrow diffraction peaks of the ball-milled A_0 alloy show a typical nanocrystalline structure and an average grain size of about 36 nm, which is calculated using Eq 2 on the basis of the Cauchy integral breadth of major diffraction peak (44.36°):

$$D = \lambda / \beta_c^f cos\theta, \quad \text{(Eq 2)}$$

where θ, λ, and β_c^f denote the diffraction angle, x-ray wavelength, and integral breadth, respectively. With the addition of TiF_3, the diffraction peaks of milled A_3 and A_5 alloys evidently broaden and diffuse, exhibiting the characteristics of amorphous and nanocrystalline structures. The TiF_3 additive helps form nanocrystalline and amorphous structures inside the milled A_0, A_3, A_5 alloys. The results of HRTEM detection are shown in Fig. 3.

The HRTEM photographs of different magnification and ED maps of the ball-milled A_0, A_3, A_5 alloys are presented in Fig. 3. The HRTEM morphologies under lower magnification indicate that the grains of the alloy sample are refined gradually with incremental TiF_3 content. The HRTEM images of higher magnification reveal that the milled A_0 alloy exhibits an

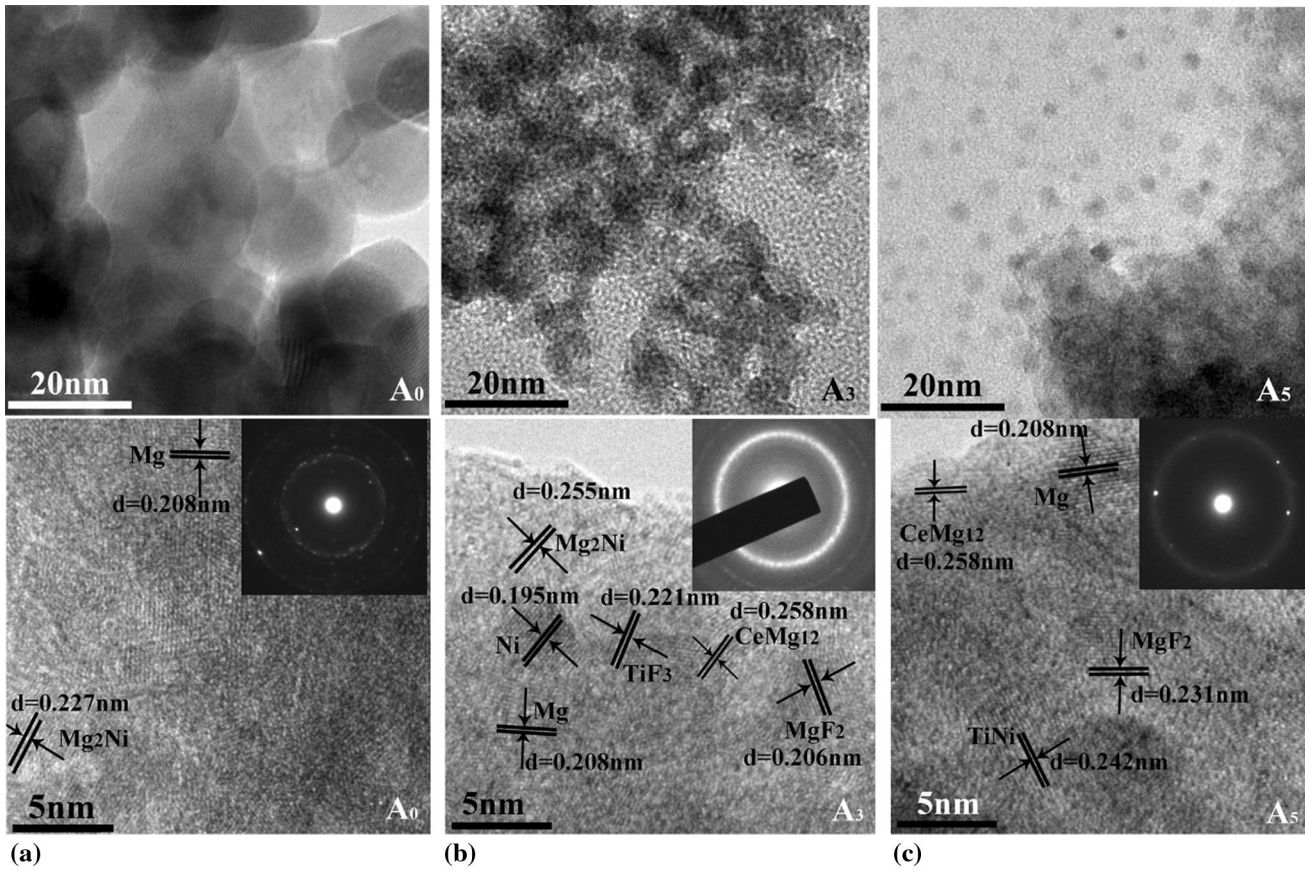

Fig. 3 HRTEM micrographs and electron diffraction (ED) maps of ball-milled A_0, A_3, and A_5 alloys: (a) A_0 alloy; (b) A_3 alloy; and (c) A_5 alloy

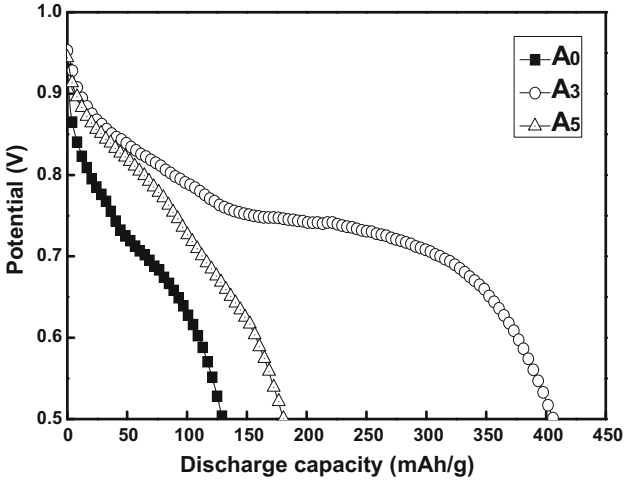

Fig. 4 Discharge curves of ball-milled A_0, A_3, A_5 alloys

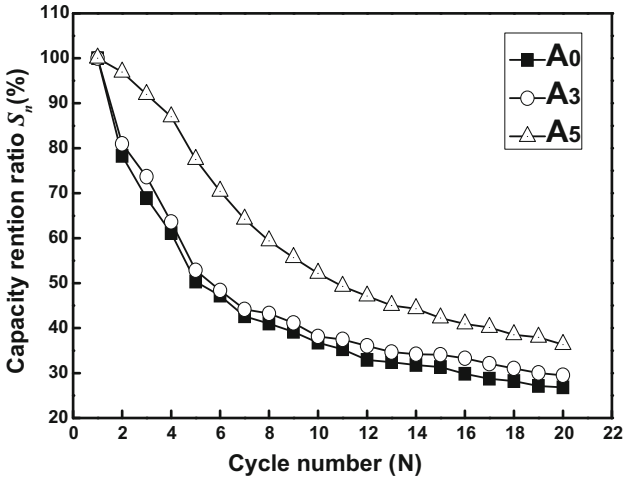

Fig. 5 Evolution of capacity retaining rate of ball-milled A_0, A_3, A_5 alloys with cycle number

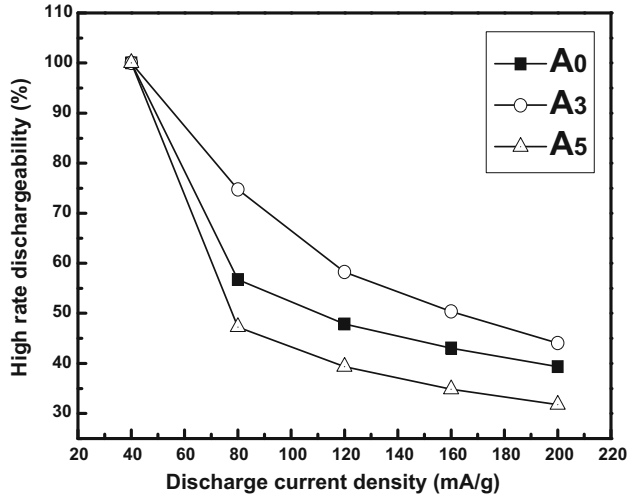

Fig. 6 High-rate dischargeability curve of the ball-milled A_0, A_3, A_5 alloys

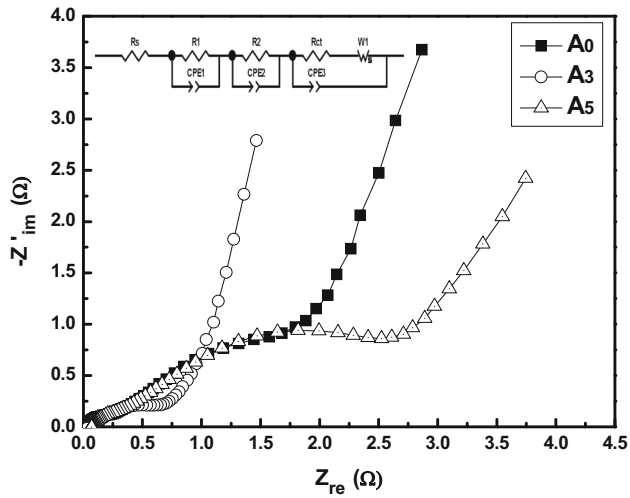

Fig. 7 Electrochemical impedance spectra (EIS) of A_0, A_3, A_5 alloys milled for 60 h

emblematic nanocrystalline structure, as indicated by sharp multi-halo electron diffraction images. The A_3 and A_5 alloys show a mixed feature of a nanocrystalline structure surrounded by an amorphous phase. The ED result verifies the presence of the amorphous structure. They further investigate the phase compositions by the interplanar spacing of different areas in HRTEM images, considering that the phase component includes small quantities of TiNi, MgF_2, TiF_3, and $CeMg_{12}$ except for Mg and Mg_2Ni for A_3 and A_5 alloys. However, the HRTEM images are used for investigating the forming ability of amorphous and nanocrystalline inside alloy samples only in literature report (Ref 21).

3.2 Electrochemical Charge/Discharge Properties

3.2.1 Discharge Performance. Figure 4 depicts the discharge plots of the ball-milled A_0, A_3, A_5 alloy electrodes at the first charge/discharge cycle. Apparently, the discharge curves of the three ball-milled alloy electrodes exhibit different discharging plateaus owing to the oxidation of hydride during hydrogen desorption. Suitable addition of TiF_3 clearly enhances the discharge potential of the ball-milled alloys. Among the three alloy samples, the A_3 alloy sample exhibits the highest discharge capacity. The internal resistance of the alloy materials leads to the variation in discharge potential. The A_3 alloy sample has the highest voltage plateau, which indicates the weakest electrochemical polarization and the strongest charge transfer ability on the surface of the alloy. The microstructural characteristic inside the A_3 alloy facilitates hydrogen diffusion and reduces polarization resistance.

The aforementioned results may have several interpretations. The addition of TiF_3 causes a microstructural change in the ball-milled alloys, which leads to a difference in their discharge voltage platform and capacity. Meanwhile, TiF_3 induces the production of MgF_2 and TiNi phases in the A_3 and A_5 alloy samples, as shown in Fig. 4. In particular, the

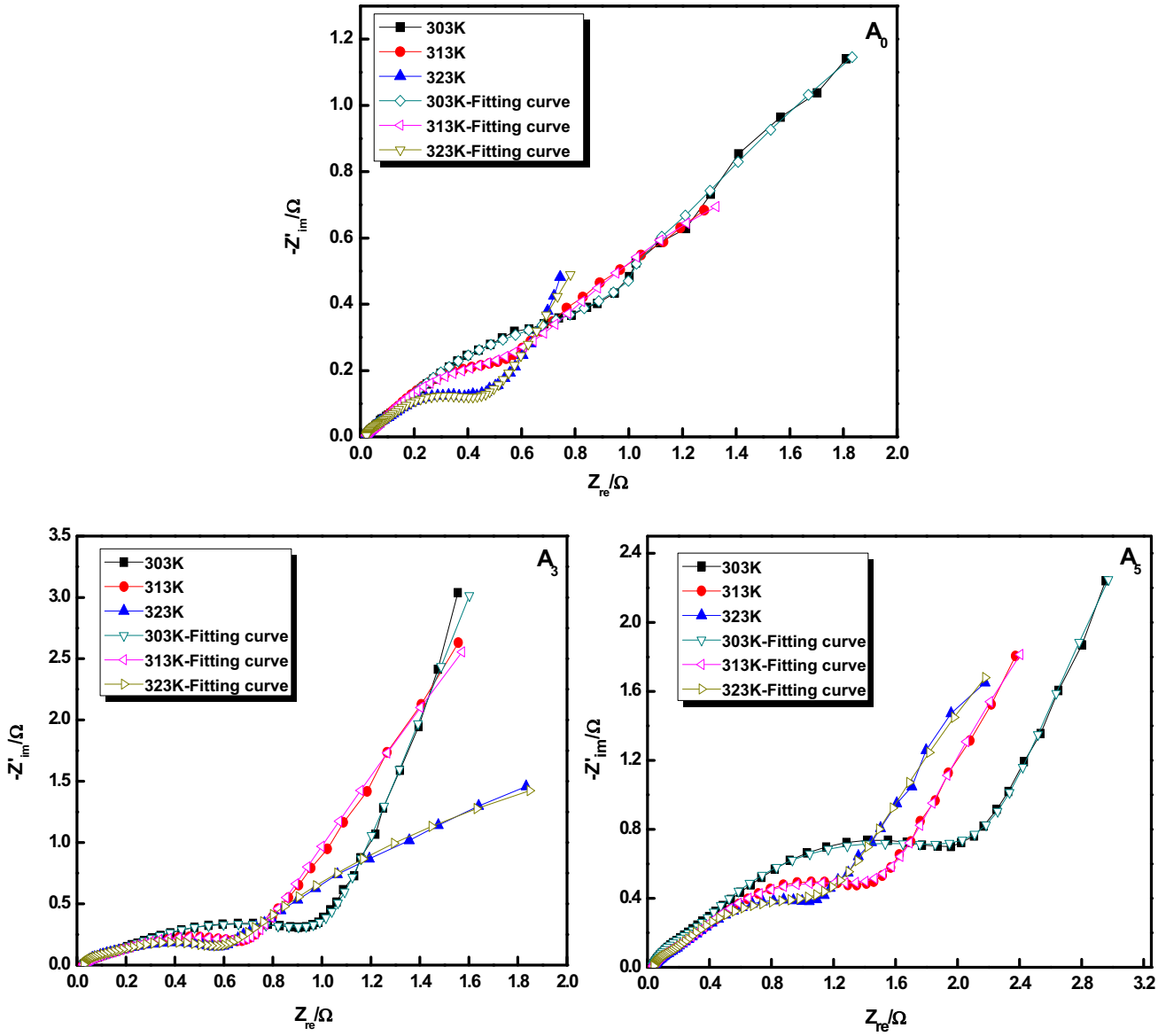

Fig. 8 EIS and fitting curves of the ball-milled A_0, A_3, A_5 electrode alloys at 303 K, 313 K, and 323 K

formation of MgF_2 can effectively reduce the thermodynamic stability and enhance the electrochemical discharge capacity of ball-milled alloys (Ref 17).

3.2.2 Electrochemical Cycling Life. The capability retention ratio (S_n) is used to characterize the electrochemical cycle stability, which can be calculated using Eq 3 as follows:

$$S_n = C_n/C_{\max} \times 100\%, \quad \text{(Eq 3)}$$

where $C_{\max}$ is the maximum discharge capacity and C_n is the discharge capacity at the nth charge–discharge cycle.

The evolution of the S_n of the A_0, A_3, A_5 alloys milled for 60 h with cycle number n is established in Fig. 5. TiF_3 can clearly help improve the decay rate of the discharge capacity. The positive effect of the TiF_3 additive on the cycling stabilization of the milled alloy electrode is attributed to the formation of an amorphous phase which can enhance the anticorrosive and antioxidation ability of the hydrogen storage alloy (Ref 18). In addition, the formation of MgF_2 and TiNi phases can benefit the electrochemical cycling life of ball-milled A_0, A_3, A_5 alloys (Ref 19).

3.3 Electrochemical Kinetic Properties

3.3.1 High-Rate Dischargeability. Figure 6 shows the HRD values of the A_0, A_3, A_5 alloy electrodes. The result shown in Fig. 6 indicates that a certain amount of TiF_3 can effectively improve the electrochemical kinetic properties of ball-milled alloy electrodes. The improved HRD is related to the appearance of an amorphous and nanocrystalline structure. This structure holds numerous crystal defects, provides effective hydrogen diffusion paths, and accelerates charge–transfer reaction (Ref 20). In addition, the formation of MgF_2 and amorphous phase is favorable for the acceleration of the charge transfer reaction on the surface of ball-milled A_3 and A_5 alloys (Ref 21).

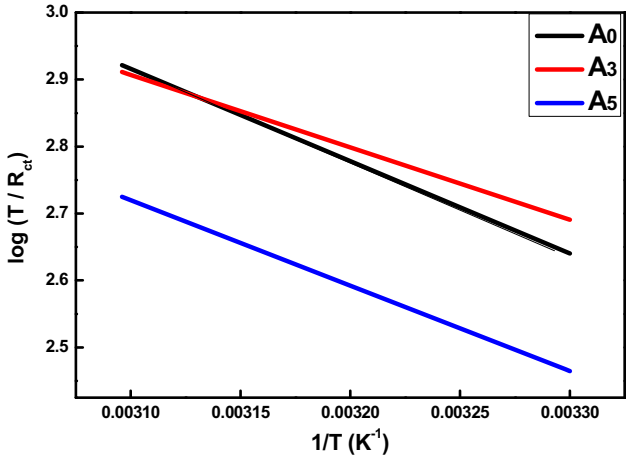

Fig. 9 Curves of log (T/R_{ct}) vs. $1/T$ of A_0, A_3, A_5 alloys milled for 60 h

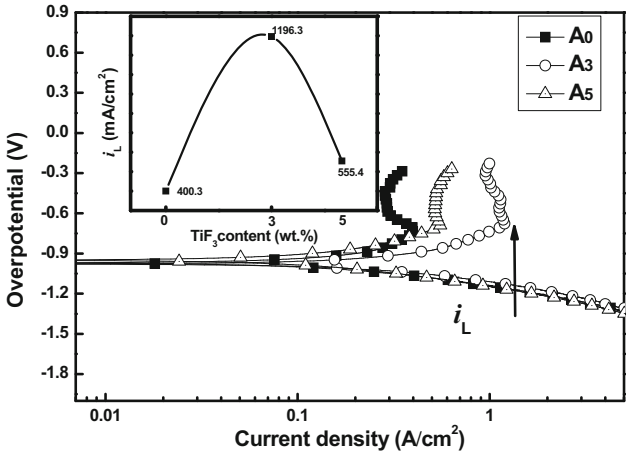

Fig. 10 Potentiodynamic polarization of A_0, A_3, A_5 alloy electrodes milled for 60 h

Table 1 Electrochemical impedance parameters and activation energies (ΔE) of A_0, A_3, A_5 alloys at different temperatures

	R_{ct}, Ω						
Sample	303 K	Error, %	313 K	Error, %	323 K	Error, %	ΔE, kJ
A_0	0.52948	6.57	0.38799	5.62	0.29263	5.44	27.163
A_3	0.42604	5.68	0.37999	5.27	0.28847	6.46	18.497
A_5	1.65013	3.61	0.93978	4.54	0.67194	6.49	38.604

R_{ct} is charge transfer resistance

3.3.2 Electrochemical Impedance Spectrum (EIS) and Potentiodynamic Polarization. The EIS of the A_0, A_3, A_5 alloy samples milled for 60 h at 50% depth of discharge (DOD) are shown in Fig. 7. The EIS of each alloy typically include two capacitive loops. According to Kuriyama, the capacitive reactance arc of the middle-frequency party represents the charge–transfer resistance from the double-layer capacitance (Ref 22).

Apparently, the curvature radius of the capacitive reactance arc of the middle-frequency party first decreases and then increases. This occurrence shows that R_{ct} of the milled alloys first shrinks and then rises with an increase in TiF_3 content. For the A_3 alloy, the decrease in R_{ct} may be attributed to the following two reasons: (1) TiF_3 facilitates the formation of an amorphous and nanocrystalline structure, which effectively decreases the charge–transfer reaction resistance and (2) the rare-earth element Ce and the Ni phase play catalytic functions in the charge–transfer reaction. However, further addition of TiF_3 can cause an increase of $Ce(OH)_3$, $Ni(OH)_2$, and $Mg(OH)_2$ oxide layer, which results in an increase in charge transfer resistance (R_{ct}) (Ref 23).

The activation energy E_a is introduced to estimate the activation properties on the alloy surface and thus investigate the surface active performance of the ball-milled A_0, A_3, A_5 alloys. E_a can be determined using Eq 4 by the fitting curves in Fig. 8:

$$\log\left(\frac{T}{R_{ct}}\right) = -\frac{E_a}{2 \cdot 303RT} + C \qquad \text{(Eq 4)}$$

The relationship curves between log (T/R_{ct}) and $1/T$ are presented in Fig. 9. The E_a of each milled alloy is listed in Table 1. The activation energy E_a initially declines and then rises as TiF_3 content increases. The result indicates that the ball-milled alloy with 3 wt.% TiF_3 additive exhibits the smallest surface activation energy, which is conducive to reduce the energy barrier of the electrochemical reaction on the surface of the alloy electrode and accelerates the charge transfer reaction.

Figure 10 illustrates the potentiodynamic polarization curves of the milled A_0, A_3, and A_5 alloy electrodes. An inflection point clearly appears on each anodic polarization curve, namely the limiting value of the current density, referred to as the limiting current density (i_L). The existence of i_L is attributed to the oxidation product, which is known to hinder further penetration of hydrogen atoms because oxidation reaction takes place on the surface of the alloy electrode. Figure 10 reveals that i_L first increases from 400.3 mA/g (A_0 alloy) to 1196.3 mA/g (A_3 alloy) and then decreases to 555.4 mA/g (A_5 alloy) with increasing TiF_3 content. The test results lead to the conclusion that the ball-milled alloy with 3 wt.% TiF_3 possesses the strongest electrochemical reaction kinetics, which suggests that the fastest mass transfer process can more efficiently satisfy the requirements for electrochemical reaction to occur. This finding results from the two observations: (1) TiF_3 enhances the ability to form nanocrystalline/amorphous structure, which increases the interface, internal strain, and grain boundary, thereby providing a diffusion path for hydrogen. Niu demonstrated that internal strain directly affected the exchange current density and hydrogen diffusion ability (Ref 24); (2) Ni exhibits the strongest electro-catalysis, which contributes to the enhancement of the diffusion capability of hydrogen atoms (Ref 25).

4. Conclusions

1. The addition of TiF_3 changes the microstructure and phase composition of ball-milled A_0, A_3, A_5 alloys, sig-

nificantly improving the electrochemical discharge capacity.

2. The higher reaction resistance of the A_5 alloy reduces the cycling decay rate of the discharge capacity, which may be attributed to the formation of the oxidation layer on the surface of the alloy and numerous amorphous or nanocrystalline structures.
3. X-ray diffraction reveals that the addition of TiF_3 is conducive to the formation of nanocrystalline and amorphous structures inside the milled A_3, A_5 alloys. Such structures have a number of crystal defects, which provide diffusion paths for hydrogen atoms. The 3 wt.% TiF_3 additive can reduce the activation energy (E_a), thus improving the electrochemical reaction kinetics of the experimental alloy samples.

Acknowledgments

This work is supported by National Natural Science Foundations of China (Grant Nos. 51161015, 51501095 and 51371094), Natural Science Foundation of Inner Mongolia, China (Grant No. 2014MS0529), Innovation Foundation of Inner Mongolia University of Science and Technology (Grant No. 2014QDL015).

References

1. I.P. Jain, C. Lal, and A. Jain, Hydrogen Storage in Mg: A Most Promising Material, *Int. J. Hydrogen Energy*, 2010, **35**, p 5133–5144
2. Y. Jia, C. Sun, S. Shen, J. Zou, S.S. Mao, and X. Yao, Combination of Nanosizing and Interfacial Effect: Future Perspective for Designing Mg-Based Nanomaterials for Hydrogen Storage, *Renew. Sustain. Energy Rev.*, 2015, **44**, p 289–303
3. K.J. Gross, D. Chartouni, E. Leroy, A. Züttel, and L. Schlapbach, Mechanically Milled Mg Composites for Hydrogen Storage: The Relationship Between Morphology and Kinetics, *J. Alloys Compd.*, 1998, **269**(1–2), p 259–270
4. H. Wang, H.J. Lin, W.T. Cai, L.Z. Ouyang, and M. Zhu, A multiband RF Signal Sampling Frequency Selection Method Based on Cylindrical Surface Spectrum Analysis, *J. Alloys Compd.*, 2016, **658**, p 280–300
5. Y.H. Zhang, Z.M. Yuan, T. Yang, D.C. Feng, Y. Cai, and D.L. Zhao, An Investigation on Hydrogen Storage Thermodynamics and Kinetics of Pr-Mg-Ni-Based $PrMg_{12}$-Type Alloys Synthesized by Mechanical Milling, *J. Alloys Compd.*, 2016, **688**, p 585–593
6. H. Fu, W. Wu, Y. Dou, B. Liu, H. Li, and Q. Peng, Hydrogen Diffusion Kinetics and Structural Integrity of Superhigh Pressure Mg-5 wt%Ni Alloys with Dendrite Interface, *J. Power Sources*, 2016, **320**, p 212–221
7. Y.Q. Lei, Y.M. Wu, Q.M. Yang, J. Wu, and Q.D. Wang, Charge/Discharge Hysteresis Characteristics of an Amorphous $Mg_{50}Ni_{50}$ Hydride Electrode, *Z. Phys. Chem.*, 1994, **183**, p 379–384
8. Y.H. Zhang, Z.H. Hou, S.H. Guo, G.F. Zhang, X. Li, and D.L. Zhao, Electrochemical Hydrogen Storage Characteristics of $(Mg_{1-x}Zr_x)_2Ni$ (x = 0-0.3) Alloys Prepared by Mechanical Alloying, *Adv. Mater. Res.*, 2011, **291–294**, p 29–34
9. K. Pal, Synthesis, Characterization and Dehydriding Behavior of the Intermetallic Compound $LaMg_{12}$, *Int. J. Hydrogen Energy*, 1997, **22**(8), p 799–804
10. Y. Chen, C. Sequeira, C.P. Chen, and Q.D. Wang, Electrochemical Properties of the Ball-Milled $La_{1.8}Ca_{0.2}Mg_{14}Ni_3$ + xwt%Ni Composites (x = 0, 50, 100 and 200), *J. Alloys Compd.*, 2003, **354**(1–2), p 120–123
11. X.P. Gao, Z.W. Lu, Y. Wang, F. Wu, D.Y. Song, and P.W. Shen, Electrochemical Hydrogen Storage of Nanocrystalline La_2Mg_{17} Alloy Ball Milled with Ni Powders, *Electrochem. Solid-State Lett.*, 2004, **7**(5), p A102–A104
12. Y. Wang, Z.W. Lu, Y.L. Wang, T.Y. Yan, J.Q. Qu, X.P. Gao, and P.W. Shen, Electrochemical Hydrogen Storage of Ball-Milled $CeMg_{12}$ and $PrMg_{12}$ Alloys with Ni Powders, *J. Alloys Compd.*, 2006, **421**(1–2), p 236–239
13. Y. Wang, S.Z. Qiao, and X. Wang, Electrochemical Hydrogen Storage Properties of Ball-Milled $NdMg_{12}$ Alloy with Ni Powders, *Int. J. Hydrogen Energy*, 2008, **33**, p 1023–1027
14. S. Deledda, A. Borissova, and C. Poinsignon, H-Sorption in MgH_2 Nanocomposites Containing Fe or Ni with Fluorine, *J. Alloys Compd.*, 2005, **404–406**, p 409–412
15. J. Charbonnier, P. de Rango, and D. Fruchart, Hydrogenation of Transition Element Additives (Ti, V) During Ball Milling of Magnesium Hydride, *J. Alloys Compd.*, 2004, **383**, p 205–208
16. S.A. Jin, J.H. Shim, and Y.W. Cho, Dehydrogenation and Hydrogenation Characteristics of MgH_2 with Transition Metal Fluorides, *J. Power Sources*, 2007, **172**, p 859–862
17. H. Chai, H. Gu, and Y.F. Zhu, Effect of TiF_3 on the Hydrogen Desorption Property of $Mg_{95}Ni_5$ by Hydriding Combustion Synthesis, *Rare Met. Mater. Eng.*, 2010, **39**, p 50–54
18. Y.H. Zhang, B.W. Li, H.P. Ren, Y. Cai, X.P. Dong, and X.L. Wang, Investigation on Structures and Electrochemical Performances of the As-Cast and -Quenched $La_{0.7}Mg_{0.3}Co_{0.45}Ni_{2.55-x}Fe_x$ (x = 0-4) Electrode Alloys, *Int. J. Hydrogen Energy*, 2007, **32**, p 4627–4634
19. J. Bicerano, J.E. Keem, and H.B. Schlegel, Theoretical Studies of Hydrogen Storage in Binary Ti-Ni, Ti-Cu and Ti-Fe Alloys, *Chim. Acta*, 1986, **70**, p 265–296
20. P.H.L. Notten and P. Hokkeling, Double-Phase Hydride Forming Compounds: A New Class of Highly Electrocatalytic Materials, *J. Electrochem. Soc.*, 1991, **138**(7), p 1877–1885
21. F. Hu, Y.H. Zhang, Y. Zhang, Z.H. Hou, Z.P. Dong, and L.B. Deng, Microstructure and Electrochemical Hydrogen Storage Characteristics of $CeMg_{12}$ + 100 wt%Ni +Ywt%TiF_3 (Y = 0, 3, 5) Alloys Prepared by Ball Milling, *J. Inorg. Mater.*, 2013, **28**(2), p 217–223
22. N. Kuriyama, T. Sakai, H. Miyamura, I. Uehara, H. Ishikawa, and T. Iwasaki, Electrochemical Impedance and Deterioration Behavior of Metal Hydride Electrodes, *J. Alloy. Compd.*, 1993, **202**(1–2), p 183–197
23. L. Wang, X.H. Wang, L.X. Chen, X.Z. Xiao, L.H. Gao, C.Y. Wang, C.P. Chen, and Q.D. Wang, Effect of Ni Content on the Electrochemical Performance of the Ball-Milled $La_2Mg_{17-x}Ni_x$ + 200wt.%Ni (x = 0, 1, 3, 5) Composites, *J. Alloys Compd.*, 2007, **428**(1–2), p 338–343
24. H. Niu and D.O. Northwood, Enhanced Electrochemical Properties of Ball-Milled Mg_2Ni Electrodes, *Int. J. Hydrogen Energy*, 2002, **27**, p 69–77
25. Y. Wang, Z.W. Lu, X.P. Gao, W.K. Hu, X.Y. Jiang, J.Q. Qu, and P.W. Shen, Electrochemical Properties of the Ball-Milled $LaMg_{10}Ni_{2-x}Al_x$ Alloys with Ni Powders (x = 0, 0.5, 1 and 1.5), *J. Alloys Compd.*, 2005, **389**(1–2), p 290–295